Title
BETA-DECAY ENERGIES AND MASSES OF 103-105In

Author
Wouters, J.M.

Publication Date
1982-02-01

LBL-13990
Preprint

Lawrence Berkeley Laboratory

UNIVERSITY OF CALIFORNIA

Submitted to Physical Review C

BETA-DECAY ENERGIES AND MASSES OF $^{103-105}$In

J.M. Wouters, H.M. Thierens, J. Aysto, M.D. Cable,
P.E. Haustein, R.F. Parry and Joseph Cerny

February 1982

NUCLEAR SCIENCE DIVISION

Prepared for the U.S. Department of Energy under Contract W-7405-ENG-48

DISCLAIMER

Beta-Decay Energies and Masses of $^{103-105}$In*

J. M. Wouters, H. M. Thierens[†], J. Äystö[††], M. D. Cable,
P. E. Haustein[†††], R. F. Parry and Joseph Cerny

Department of Chemistry and Lawrence Berkeley Laboratory,
University of California, Berkeley, CA 94720

Abstract: Decay energies of $^{103-105}$In have been determined by β-γ coincidence spectroscopy on sources obtained from the on-line mass separator RAMA. Comparisons of the measured decay energies and deduced masses are made with the predictions of several different theoretical models. The ^{103}In mass is found to be more bound by 1 MeV than predicted by most models, which reproduce adequately the masses of the heavier indium isotopes. Systematic trends of the masses and neutron separation energies of the indium isotopes between the closed N=50 and 82 shells are presented.

RADIOACTIVITY: $^{103-105}$In [from Mo(^{14}N,xn), Mo(^{16}O,pxn)]; measured $E_{\beta+}$, $\beta\gamma$ coin; deduced Q_{EC}, mass excesses. On-line mass separation; enriched and natural targets; Ge(Li), scintillator telescope detectors; response function correction E-scintillator.

†Present address: University of Gent, Belgium.
††Permanent address: University of Jyväskylä, Finland.
†††Permanent address: Brookhaven National Laboratory, Upton, NY, USA.
*This work was supported by the Director, U.S. Office of Energy Research, Division of Nuclear Physics of the Office of High Energy and Nuclear Physics, and by Nuclear Sciences of the Basic Energy Sciences Program of the U.S. Department of Energy under Contract No. W-7405-ENG-48.

I. Introduction

An extension of the experimentally known nuclidic mass surface to nuclei far from the region of β-stability is of fundamental interest in providing a better determination of the input parameters for the various nuclear mass formulae, allowing a more accurate prediction of the limits of nuclear stability. In addition, a study of the shape of the mass surface in the vicinity of the doubly-closed nuclide ^{100}Sn provides information on the strength of the shell closure to be expected when Z=N=50. Recently, masses of highly neutron-deficient nuclei in this region, especially Sn and Te isotopes such as ^{105}Sn and ^{109}Te, were deduced by Plochocki et al.[1] from measurements of $\beta^+/(EC+\beta^+)$ decay probability ratios and mass difference data from particle spectroscopy studies.

As a further step in the extension of the mass surface we have determined the decay energies for $^{103-105}In$ by β-endpoint measurements with mass separated samples from the mass separator RAMA[2-4], located on-line at the Lawrence Berkeley Laboratory 88-inch Cyclotron. The experimentally determined decay energies and derived masses for $^{103-105}In$ are compared with the predictions of different mass models to identify which models are more successful in this region. Further, the inclusion of the available data on the neutron-rich indium nuclei in these comparisons permits a systematic study of the ground state mass behavior of these isotopes as a function of the neutron number between the shell closures at N=50 and 82. An examination of single- and two-neutron separation energies in the vicinity of $^{103-105}In$ is also performed to investigate possible systematic variations in the mass surface in a model-independent way.

II. Experiment

Heavy-ion beams of ^{12}C, ^{14}N and ^{16}O were directed onto various targets to produce the isotopes of interest via (HI,xn) and (HI,pxn) reactions. More specifically, ^{103}In was produced via the $^{92}Mo(^{14}N,3n)$ and $^{92}Mo(^{16}O,p4n)$ reactions with beam energies of 80 and 115 MeV, respectively; ^{104}In was produced via the $^{92}Mo(^{16}O,p3n)$ reaction at 95 MeV: and ^{105}In was produced via the $^{nat}Mo(^{14}N,xn)$ and $^{92}Mo(^{16}O,p2n)$ reactions with beam energies of 100 and 75 MeV, respectively. All targets were ~2 mg/cm^2 thick: the average beam intensity varied between 2 and 4 eμA. To improve the yield at a given beam energy, two identical targets were used simultaneously in conjunction with a multiple capillary system. The nuclear reaction recoils were thermalized behind each target in 1.5 atmospheres of helium, collected by the multiple capillary system and transported via a helium-jet to the hollow-cathode ion source of the mass separator RAMA[2-4]. The mass-analyzed 18 keV ion beam was implanted onto mylar tape during a suitable collection interval, and rapidly transported (<250 msec) to a detector station configured for β singles and β-γ coincidence spectroscopy. (See Fig. 1.)

The detector station consisted of a scintillator telescope, positioned facing the source side of the tape, for β counting and a 15% Ge(Li) detector, located on the opposite side of the tape, for γ counting. The β-telescope comprised a 10 mm diameter and 1 mm thick NE102 plastic scintillator as a ΔE counter (for γ-ray rejection) and a large cylindrical NE102 plastic scintillator, 11.4 cm in both diameter and length, as an E detector. Standard fast-slow coincidence networks were appropriately set up using the three detectors so that both β-singles spectra as well as β-γ coincidence spectra could be obtained. The final coincidence timing of 5 ns (FWHM) between the two scintillators and 20 ns (FWHM) between the β-E scintillator and the Ge(Li) counter greatly reduced chance coincidences between detectors at the modest maximum singles counting rate (<2000 counts/second) in each detector. Multiparameter events were stored sequentially on magnetic tape using the CHAOS[5)] (now called MINUS 3) acquisition and analysis FORTRAN code running on a ModComp IV computer.

Positron spectra, coincident with known transitions in the daughter nuclei, were subsequently obtained by software gating the coincidence event data with the appropriate γ-rays and subtracting background β-spectra obtained from "off peak" γ-ray gates. Energy endpoint determinations were then calculated from appropriately weighted linear least-squares fits to Fermi-Kurie plots of the data after correcting for the finite energy resolution of the E scintillator. This correction is calculated by assuming a theoretical shape, T(E), for the β-spectrum with endpoint energy

E_0 and distorting it using a semi-empirically derived response function, R(E,E'), for the E detector. This procedure, initially suggested by Rogers and Gordon[6], yields an energy-dependent correction factor, K(E), by which the measured β-spectrum is multiplied. Following Beck[7] and Otto et al.[8], a Gaussian response function was employed with a $\sqrt{E}$ dependence for the FWHM. This FWHM was determined to be 200 keV at 976 keV by using the conversion electrons from ^{207}Bi. The overall correction factor, K(E), can thus be written as:

$$K(E) = T(E)/\left[\int^{E_0} T(E')R(E,E')dE'\right] \tag{1}$$

with the response function given by:

$$R(E,E') = \frac{1}{\sigma_1\sqrt{2\pi E'}}\, e^{-(E-E')^2/2\sigma_1^2 E'} \tag{2}$$

where σ_1 is a proportionality constant.

A two-step procedure was used for calculating the error in the individual endpoints. A statistical error was determined using the formalism of Rehfield[9] which weights the Fermi-Kurie plot by the factor

$$\omega_i \equiv 1/\sigma_i^2 = 4p_i F_i E_i \tag{3}$$

and determines the error in the endpoint to be

$$\sigma_{E_o}{}^2 = \frac{1}{A^2\Delta} \sum (E_o - E_i)^2/\sigma_i{}^2 \qquad (4)$$

with

$$\Delta = \sum \frac{1}{\sigma_i{}^2} \sum \frac{E_i{}^2}{\sigma_i{}^2} - \left(\sum \frac{E_i}{\sigma_i{}^2}\right)^2 \qquad (5)$$

In these expressions F_i is the Fermi function, p_i the momentum and E_i the energy corresponding to channel i. The slope and endpoint of the Fermi-Kurie plot are indicated by A and E_o. The range of the summations is determined by the limits of the least-squares fit. This statistical error was adjusted by accounting for the variation in the endpoint with shifts in the energy limits over which the least-squares fit was performed. The statistical error was then added quadratically to the error due to the energy calibration of the β telescope to obtain the final error in the endpoint.

$$\sigma^2_{E_{Calibration}} = \sum_i^N \left\{\sigma^2_{Lit_i}\left(\chi_o \frac{\partial f_A}{\partial E_i} + \frac{\partial f_B}{\partial E_i}\right)^2 + \sigma^2_{FK_i}\left(\chi_o \frac{\partial f_A}{\partial \chi_i} + \frac{\partial f_B}{\partial \chi_i}\right)^2\right\} \qquad (6)$$

$$f_A = f_A(E_i, \chi_i)$$

$$f_B = f_B(E_i, \chi_i)$$

In equation 6 the slope f_A and the intercept f_B of the calibration function depend on the literature values for the endpoints of the calibration nuclei E_i with uncertainties σ_{Lit_i} and the corresponding measured channel numbers χ_i with errors σ_{FK_i}. The channel number corresponding to the calculated endpoint energy E_0 is indicated by χ_0 and N is the number of calibration nuclei.

Figure 2a presents the Fermi-Kurie plot from the decay of ^{38}K, one of the calibration nuclei, with the appropriate error bars as an example of the weighted linear least-squares fits obtained. The energy calibration as determined using the calibration activities[10,11] listed in Table I was found to give a good linear fit (see Fig. 2b). Table I also presents for each calibration activity the γ-gate employed to obtain the β-spectrum and the reaction used for the production of the activity.

III. Results

The final results of our experiments are presented in Table II, which lists the γ-rays and their relative intensities as observed following the β-decay of ^{103}In, and Table III, which lists the calculated Q_{EC}s of $^{103-105}In$. Close examination of the γ-spectrum of ^{103}In in coincidence with β's revealed two γ-rays at 720 and 740 keV, decaying with the proper half life of 60.5s, in addition to the 188 keV and 202 keV γ-rays observed previously by Lhersonneau et al.[12]. The observation of these γ-rays is in agreement with the recent results of Béraud et al.[13] although the relative intensities of 32 and 19% which are quoted for the 720 and 740 keV γ-rays, respectively, are slightly higher than our results indicate. Based on the reaction work of Meyer et al.[14], the 720 keV γ-ray corresponds to the first member of a decoupled band based on the 188.1 keV $7/2^+$ state.

The Fermi-Kurie analysis of the positron spectrum from ^{103}In in coincidence with the 188 keV γ-transition in the ^{103}Cd daughter is shown in Fig. 3a. A partial decay scheme for ^{103}In is also given in this figure with the beta branching ratios determined from the measured relative γ-intensities. Figure 3a shows that the linearity of the Fermi-Kurie plot is not affected seriously by the small β-feeding of the $11/2^+$ level.

The decay scheme of ^{104}In has been studied intensively by Huang et al.[15] According to these authors about 22% of the beta decay feeds the second excited state (4^+) at 1492 keV, while the first excited state (2^+) at 658 keV is not fed directly. All the higher-lying levels deexcite via the 4^+ level by γ-ray emission. Since approximately 50% of the β-decay strength feeds three close-lying states at 2370.2, 2435.4 and 2492.3 keV, the energy range for the least squares fit in the Fermi-Kurie plot is restricted to the highest 1 MeV of the data. Figure 3b presents the Fermi-Kurie analysis for the ^{104}In positron singles spectrum together with a partial decay scheme for ^{104}In. Positron spectra in coincidence with the 658 keV and 834 keV γ-rays yield, within errors, the same β-endpoint energy but have lower statistics.

According to Wischnewski et al.[16)], about 27% of the β-decay of ^{105}In feeds the first excited level at 131 keV in ^{105}Cd, while the next strongly fed levels, decaying to the 131 keV state, lie at 770 and 799 keV with β branches of 8 and 9%, respectively. The resulting partial decay scheme and Fermi-Kurie analysis of the positron spectrum in coincidence with the 131 keV γ-ray are shown in Fig. 3c.

The results of the Fermi-Kurie analysis for $^{103-105}$In are summarized in Table III. The measured β-endpoint energies, E_{max}, along with the γ-rays used for gating and the deduced Q_{EC} values are given. In addition, the decay energies previously reported in the literature are included in the table for comparison. The decay energies obtained for $^{103-104}$In agree well with the literature values; for ^{103}In the uncertainty in the Q_{EC} value is substantially reduced. A Q_{EC} value for ^{105}In was not previously available.

IV. Discussion

The decay energy measurements for $^{103-105}$In, reported in this work, can be analyzed in different ways to investigate the mass surface in this region of nuclei. A comparison of the measured decay energies with the predictions of the currently available mass theories can evaluate the reliability of these models in predicting the curvature of the mass surface. Conversion of the Q_{EC} values to mass excesses using the known masses of the cadmium isotopes also provides a direct comparison of the absolute mass excesses with the model mass predictions. Direct model-independent information on variations in the mass surface for these indium isotopes can be obtained from an examination of the neutron binding energy systematics in the vicinity of the measured nuclei.

The differences between the measured decay energies and the predictions derived from selected mass models for the neutron-deficient indium isotopes are depicted graphically in Fig. 4. To observe more easily the systematic trends, this comparison is extended to ^{110}In. (The decay energies for $^{106-110}$In are adopted from Wapstra and Bos[17)]. Each arrow in the figure is labeled by a number corresponding to the prediction of a given model. In addition to the different mass formulae presented in ref. 18, the droplet calculations of Möller and Nix[19)] are also included.

Figure 4 shows that the results of the shell model calculations of Liran-Zeldes[18d)] and the mass formulae, based on the Garvey-Kelson type relationships, of Jänecke[18e)], Comay-Kelson[18f)] and Jänecke-Eynon[18g)], reproduce very well the measured decay energies for $^{105-110}$In. In this region the droplet model predictions of Myers[18a)], Groote et al.[18b)], Seeger and Howard[18c)] and Möller and Nix[19)] are systematically too poorly bound. Beginning with ^{104}In and continuing to ^{103}In, both types of mass theories exhibit a sudden downward shift of 1 MeV so that the Liran-Zeldes and Garvey-Kelson type relationships now predict a Q_{EC} which is 1 MeV too large while those of the droplet model are at this point more accurate.

The mass excesses of $^{103-105}$In, deduced from the measured Q_{EC} values using the accurately known cadmium masses[1,15,20], are listed in Table IV. A direct comparison of the experimental masses with the different model mass predictions is also included in the table. From Table IV, it is apparent that none of these mass formulae adequately predicts the experimentally-observed mass behavior for $^{103-105}$In. Mass theories which reproduce the experimental mass of ^{105}In (i.e., Groote et al., Liran-Zeldes, Comay-Kelson and Jänecke-Eynon) place the ^{103}In mass 1 MeV less bound than is experimentally observed.

Given the sudden deviation in the ^{103}In experimental mass compared to these predictions and given its proximity to the double shell closure at ^{100}Sn, a comparison of the systematics of the ground state mass behavior for the very neutron-rich indium isotopes near the shell closure at N=82 is of related interest. Aleklett et al.[21] have studied the masses of $^{120-129}$In. For the mass excess of the closed neutron shell nucleus ^{131}In, a value of -68.55 ± 0.24 MeV can be calculated from the recently reported decay energies of ^{131}In (ref. 22) and ^{131}Sn (ref. 23) and the measured mass of ^{131}Sb (ref. 24). (The masses of the indium isotopes, not explicitly mentioned here, were adopted from ref. 17.)

In Fig. 5 the experimental indium masses for isotopes between the shell closures at N=50 and N=82 are compared to the predictions of selected, representative mass theories. The lower part of this figure compares shell and independent particle mass formulae; the upper part compares different liquid drop model predictions. The central part of the mass data between N=57 and N=76 is reproduced by the shell model of Liran-Zeldes[18d)] and the mass formulae based on the Garvey-Kelson relations[18,e,f,g)]; the root-mean-square (rms) deviation of theory from experiment in this region is less than 200 keV for each of these mass models. Approaching the closed N=82 shell, the different mass predictions diverge slowly. The model of Comay-Kelson[18f)] exhibits the best predictive qualities taking into account all of the indium data; the rms deviation from all the measured masses is only 240 keV. For the models of Liran-Zeldes[18d)], Jänecke[18e)] and Jänecke-Eynon[18g)], the corresponding values are 320, 320 and 630 keV, respectively.

From Fig. 5 it is also clear that the different droplet models, considered in this work, do not predict the masses of the indium isotopes in the region near β stability with the same accuracy as the Liran-Zeldes mass formula and the models based on the Garvey-Kelson type mass relations. One should remember, however, that the number of input parameters used for the droplet models is far fewer than for the other mass formulae. Near the N=50 and N=82 closed shells the differences between the experimental and calculated mass values for the droplet and Garvey-Kelson type mass formulae are of the same order. Among the droplet models, the best fit to the experimental data over the known mass range is obtained with the model of Möller and Nix; the rms deviation is 630 keV. In the case of the mass formulae of Myers, Groote et al., and Seeger and Howard this deviation is 1060, 820, and 780 keV, respectively. Finally, the differences between the experimental masses and the various droplet model predictions also show the sharp, systematic drop at mass 103.

As already mentioned, an examination of single- and two-nucleon separation energies can highlight systematic variations of the mass surface in a model-independent way. Figure 6a shows the behavior of the single-neutron separation energy, S_n, as a function of the neutron number for the indium isotopes. In addition to the normal odd-even oscillations, the S_n plot exhibits an irregular drop for N=55 and N=56. Both S_n values are about 0.5 MeV lower than those estimated from the systematics of Wapstra and Bos[17], which are indicated in the figure by dashed lines. Since the mass of ^{105}In is in agreement with the estimate of Wapstra and Bos, the observed deviations reflect the fact that the masses of ^{104}In and ^{103}In are, respectively, 0.5 and 1.0 MeV lower than expected from systematics. From Fig. 6a it is apparent that a similar effect is not present for the neutron-rich indium isotopes near the closed N=82 shell.

Since the neutron pairing energy is closely related to a quantity Δ_n, which can be derived from single neutron separation energies using the relationship[25)]

$$\Delta_n = \frac{(-1)^N}{4} [2S_n(N,Z) - S_n(N+1,Z) - S_n(N-1,Z)]$$

a comparison of the experimental behavior of Δ_n with the values of the different liquid drop models is informative. The variation of Δ_n for the measured indium isotopes is presented in Fig. 6b by the dots with error bars. Excluding the values for N=56 and N=57, where S_n shows an irregular behavior, Δ_n is found to fluctuate between 0.95 and 1.15 MeV, resulting in a mean value Δ_n of 1.04±0.06 MeV. Comparison with the Δ_n values of the models of Myers[18a)] and Groote et al.[18b)] indicates that the pairing terms in these models, which both basically employ the phenomenological $A^{-1/2}$ mass dependence, are slightly too low. These mass formulae predict mean values Δ_n of 0.94 and 0.92 MeV, respectively. On the other hand, the models of Seeger and Howard[18c)] and Moller and Nix[19)], which use the BCS formalism to calculate the pairing correction, seem to yield pairing terms which are too high. Mean values Δ_n of 1.26 and 1.28 MeV, respectively, are obtained using these macroscopic-microscopic approaches.

The two-neutron separation energies S_{2n} are plotted in Fig. 7 versus neutron number in the region of the indium isotopes near the closed N=50 shell. In the S_{2n} plots, the odd-even oscillations are filtered out. The recently published masses of ^{97}Pd (ref. 26), ^{98}Pd (ref. 27), ^{100}Ag (ref. 28), ^{103}Cd (ref. 20), ^{104}Cd (ref. 1) and ^{106,108}Sn (ref. 1) were also used to calculate S_{2n} values. The dashed line in the figure indicates the S_{2n} behavior according to the systematics of Wapstra and Bos[17)]. Except for the well known discontinuity corresponding to the N=50 closed shell, Fig. 7 only shows a strong deviation from the systematics for the neutron-deficient indium isotopes.

In view of the proximity of the doubly closed shell at ^{100}Sn and the reported systematics of the 2^+ and 4^+ levels for the light even cadmium isotopes[13)], it is difficult to attribute the observed irregular mass behavior of ^{103}In and ^{104}In to a sudden change in nuclear deformation as is present in the rare earth region[29)]. A further extension of the experimentally known nuclidic mass surface towards ^{100}Sn will show whether the extra binding energy of ^{103}In and ^{104}In can be explained by an increase of the proton binding energy when approaching the closed N=50 shell. Such mutual enforcement of proton and neutron magicity is present in the lead region[30)], for example, but is not observed for the very neutron rich indium isotopes near the doubly closed shell nucleus ^{132}Sn.

V. Conclusion

A direct comparison of the masses of $^{103-105}$In with the predictions of different available mass models shows that ^{103}In is about 1 MeV more bound than was expected. This conclusion is especially valid for the model of Liran-Zeldes[18d)] and several based on Garvey-Kelson type relations[18e,f,g)], which predict reasonably well the masses of the heavier indium isotopes. In addition, the irregular behavior of the single- and two-neutron separation energies for the very neutron-deficient indium isotopes reveals, in a model-independent fashion, that the ^{103}In and ^{104}In masses are lower than expected from the mass systematics of the heavier indium isotopes. Additional systematic study of the mass surface in the vicinity of ^{100}Sn is necessary to investigate whether the observed deviations are related to the nearby Z=N=50 shell closures.

This work was supported by the Director, U.S. Office of Energy research, Division of Nuclear Physics of the Office of High Energy and Nuclear Physics, and by Nuclear Sciences of the Basic Energy Sciences Program of the U.S. Department of Energy under Contract No. W-7405-ENG-48.

References

1) A. Plochocki, G. M. Gowdy, R. Kirchner, O. Klepper, W. Reisdorf, E. Roeckl, P. Tidemand-Petersson, J. Zylicz, U. J. Schrewe, R. Kantus, R. D. von Dincklage and W. D. Schmidt-Ott, Nucl. Phys. A332, 29 (1979).

2) D. M. Moltz, R. A. Gough, M. S. Zisman, D. J. Vieira, H. C. Evans, and J. Cerny, Nucl. Instr. Meth. 172, 507 (1980).

3) D. M. Moltz, J. M. Wouters, J. Äystö, M. D. Cable, R. F. Parry, R. D. von Dincklage and J. Cerny, Nucl. Instr. Meth. 172, 519 (1980).

4) D. M. Moltz, J. Äystö, M. D. Cable, R. F. Parry, P. E. Haustein, J. M. Wouters and J. Cerny, Nucl. Instr. Meth. 186, 141 (1981).

5) C. C. Maples and J. Sivak, IEEE Transactions in Nuclear Science NS-26, 4409 (1979).

6) P. C. Rogers and G. E. Gordon, Nucl. Instr. Meth. 37, 259 (1965).

7) E. Beck, Nucl. Instr. Meth. 76, 77 (1969).

8) H. Otto, P. Peuser, G. Nyman and E. Roeckl, Nucl. Instr. Meth. 166, 507 (1979).

9) D. M. Rehfield, Nucl. Instr. Meth. 157, 351 (1978)

10) C. M. Lederer and V. S. Shirley, editors, Table of Isotopes, 7th edition, John Wiley and Sons, New York, 1978.

11) M. Epherre, G. Audi, C. Thibault, R. Klapisch, G. Huber, F. Touchard and H. Wollnik, Phys. Rev. C19, 1504 (1979).

12) G. Lhersonneau, G. Dumont, K. Cornelis, M. Huyse and J. Verplancke, Phys. Rev. C18, 2688 (1978).

13) R. Béraud, J. Tréherne, A. Charvet, R. Duffait, A. Emsallem, J. Genevey, A. Gizon, J. Gizon, and M. Meyer, in Proceedings of the 4th International Conference on Nuclei Far From Stability, 1981 CERN Report 81-09, p. 692.

14) M. Meyer, R. Béraud, A. Charvet, R. Duffait, J. Tréherne, and J. Genevey, Phys. Rev. C22, 589 (1980).

15) H. Huang, B. P. Pathak and J. K. P. Lee, Can. J. Phys. 56, 936 (1978).

16) I. N. Wischnewski, H. V. Klapdor, P. Herges, H. Fromm and W. A. Zheldonozhski, Z. Physik A298, 21 (1980)

17) A. H. Wapstra and K. Bos, At. Data Nucl. Data Tables 19, 177 (1977).

18) a) W. D. Myers, At. Data Nucl. Data Tables 17, 411 (1976).
b) H. V. Groote, E. R. Hilf and K. Takahashi, ibid.. 418.
c) P. A. Seeger and W. M. Howard, ibid. 428.
d) S. Liran and N. Zeldes, ibid. 431.
e) J. Jänecke, ibid. 455.
f) E. Comay and I. Kelson, ibid. 463.
g) J. Jänecke and B. P. Eynon, ibid. 467.

19) P. Möller and J. Nix, Los Alamos National Laboratory Report LA-UR-80-1996.

20) R. C. Pardo, E. Kashy, W. Benenson and L. W. Robinson, Phys. Rev. C18, 1249 (1978).

21) K. Aleklett, E. Lund and G. Rudstam, Phys. Rev. C18, 462 (1978).

22) L. E. DeGeer and G. B. Holm, Phys. Rev. C22, 2163 (1980).

23) U. Keyser, H. Berg, F. Münnich, K. Hawerkamp, H. Schrader, B. Pfeiffer and E. Monnand, Z. Physik A289, 407 (1979).

24) E. Lund, K. Aleklett and G. Rudstam, Nucl. Phys. A286, 403 (1977).

25) S. G. Nilsson and O. Prior, K. Dan. Vidensk. Selsk. Mat. Fys. Medd. 32, No. 16 (1961).

26) H. Göktürk, N. K. Aras, P. Fettweis, P. Del Marmol, J. Vanhorenbeeck and K. Cornelis, Nucl. Phys. A344, 1 (1980).

27) C. E. Thorn, P. D. Bond, M. J. Levine, W. F. Piel and A. Gallmann, Bull. Am. Phys. Soc. 23, 72 (1978).

28) H. I. Hayakawa, I. Hyman and J. K. P. Lee, Phys. Rev. C22, 247 (1980).

29) H. E. Duckworth, R. C. Barber, P. Van Rookhuysen, J. D. Macdougall, W. McLatchie, S. Whineray, R. L. Bishop, J. O. Meredith, P. Williams, G. Southon, W. Wong, B. G. Hogg, and M. E. Kettner, Phys. Rev. Lett. 23, 592 (1969).

30) K. H. Schmidt, W. Faust, G. Münzenberg, H. G. Clerc, W. Lang, K. Pielenz, D. Vermeulen, H. Wohlfarth, H. Ewald and K. Güttner, Nucl. Phys. A318, 253 (1979).

Table I. Calibration Nuclei

Nuclide	Half-life	Gate (keV)	E_{max} (MeV)	Reaction
^{38}K	7.6 min.	2168	2.724±0.002	$^{24}Mg(^{16}O,pn)$
^{62}Cu	9.7 min.	511	2.927±0.005	$^{52}Cr(^{12}C,pn)$
^{123}Cs	5.9 min.	98	3.410±0.122	$^{nat}Cd(^{14}N,xn)$
^{66}Ga	9.4 hr.	511	4.153±0.004	$^{52}Cr(^{16}O,pn)$
^{124}Cs	31 sec.	354	4.573±0.150	$^{nat}Cd(^{14}N,xn)$

Table II. Relative Intensities of the γ-Rays in the Decay of ^{103}In

E_{γ} (keV)	I_{γ}
188	100
202	16±3
720	18±3
740	13±2

Table III. Summary of the Q_{EC} Determinations

Nuclide	Gate(s) (keV)	E_{max} (MeV)	Q_{EC}(MeV) This Work	Q_{EC}(MeV) Literature
^{103}In	188	4.17±0.13	5.38±0.13	5.8±0.5 (ref. 12)
^{104}In	658,834 NO GATE	4.91±0.14	7.42±0.14	7.1±0.2 (ref. 15)
^{105}In	131	3.99±0.13	5.14±0.13	---

Table IV. Summary of Experimental Mass Excesses and Comparison with Different Model Mass Predictions

Nuclide	Mass Excess (MeV)	$M_{exp}-M_{calc}$ (MeV)							
		a	b	c	d	e	f	g	h
^{103}In	-75.24±0.12	0.67	-1.02	0.76	-0.73	-1.20	-0.81	-0.81	-1.13
^{104}In	-76.30±0.13	1.01	-0.49	1.30	-0.10	-0.57	0.19	-0.06	-0.18
^{105}In	-79.20±0.12	1.23	-0.08	1.90	0.46	0.26	0.57	0.38	0.26

a) Myers[18a)], b) Groote et al.[18b)]; c) Seeger-Howard[18c)]; d) Möller-Nix[19)]; e) Liran-Zeldes[18d)]; f) Jänecke[18e)]; g) Comay-Kelson[18f)]; h) Jänecke-Eynon[18g)].

Figure Captions

1) Schematic view of the β-γ detector station.

2a) Fermi-Kurie plot of the ^{38}K positron spectrum in coincidence with the 2168 keV γ transition in the daughter.

2b) The energy calibration for the beta telescope using the calibration activities listed in Table II.

3) The Fermi-Kurie plots and partial decay schemes for a) ^{103}In, b) ^{104}In and c) ^{105}In.

4) Comparison of the experimental Q_{EC} values with the predictions of several model mass formulae for $^{103-110}In$. See text.

5) Comparison of the experimental masses of all the known indium isotopes with the predictions of several representative model mass formulae.

6a) Plot of single-neutron separation energies versus neutron number. Upper line is for even N isotopes while lower is for odd N ones. Dashed lines are S_n values expected from Wapstra and Bos[17)] systematics.

6b) Plot of experimental and droplet model predicted Δ_n values versus neutron number.

7) Plot of the experimental two-neutron separation energies S_{2n} versus neutron number for elements with Z=40 to 50 near the closed neutron shell at N=50. See text.

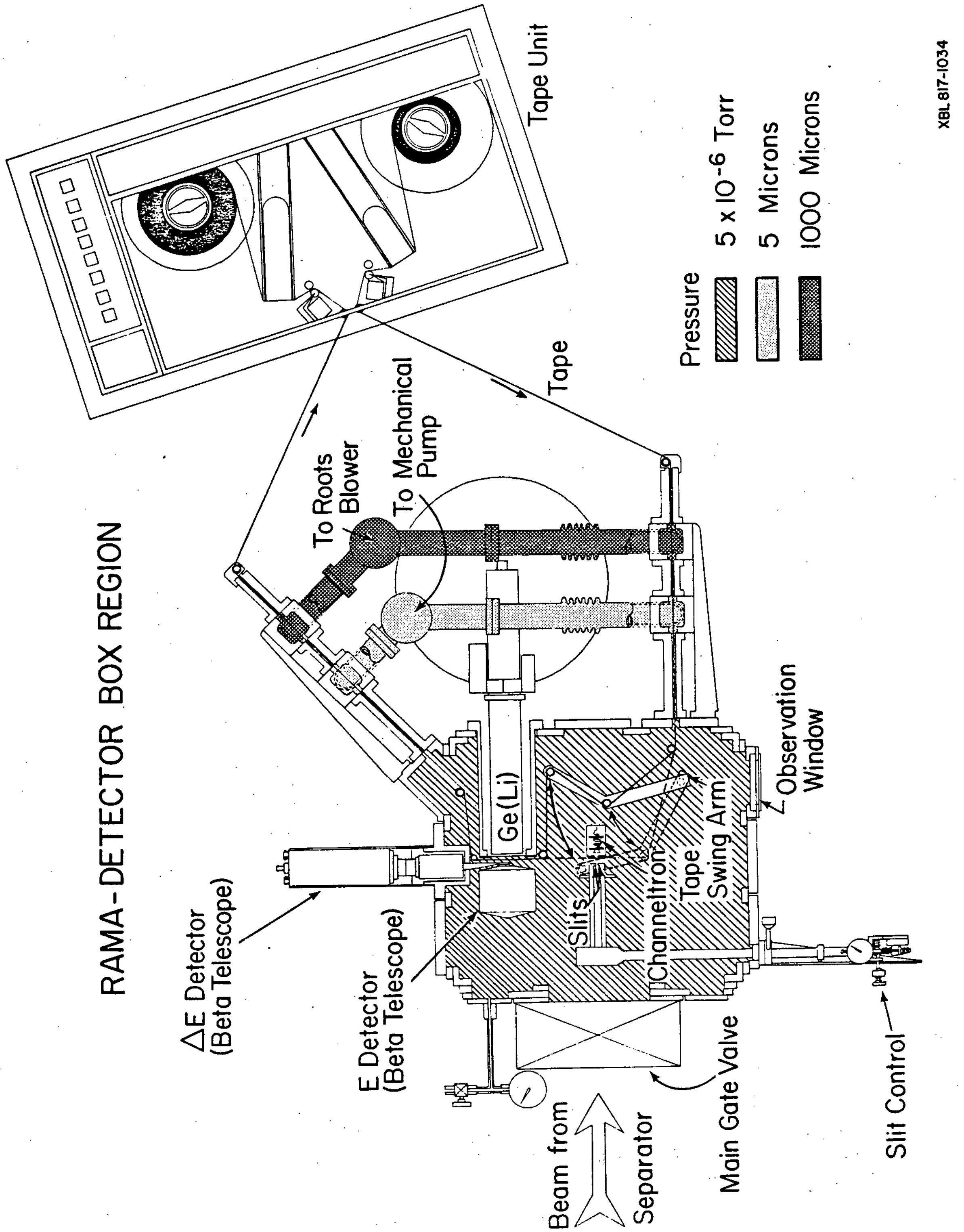
RAMA-DETECTOR BOX REGION
Tape Unit
Tape
To Roots Blower
To Mechanical Pump
Pressure
5 x 10^-6 Torr
5 Microns
1000 Microns
ΔE Detector (Beta Telescope)
E Detector (Beta Telescope)
Ge(Li)
Slits
Channeltron
Tape Swing Arm
Observation Window
Beam from Separator
Main Gate Valve
Slit Control
XBL 817-1034

Fig. 1

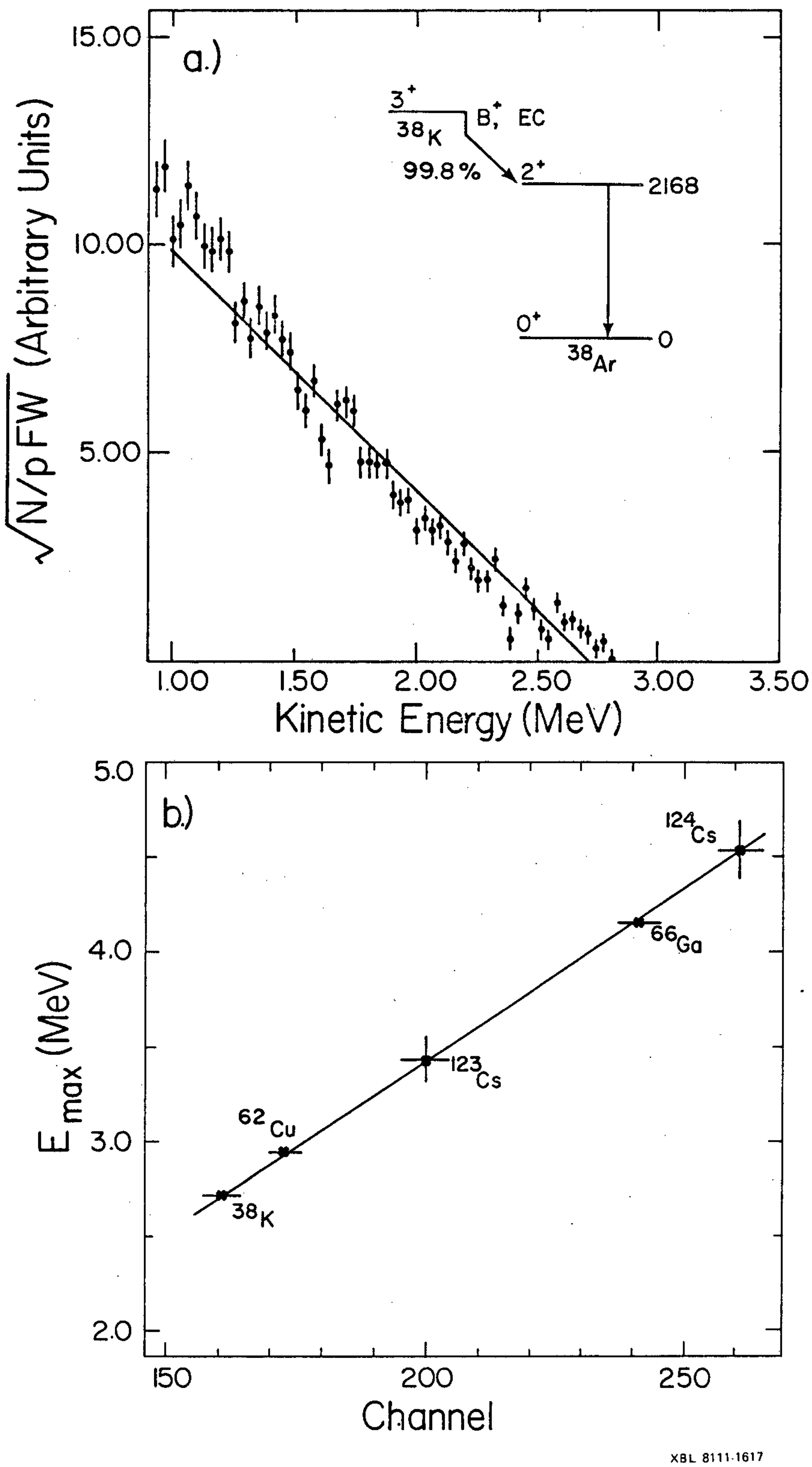
a.)
3+
38K
B+, EC
99.8 %
2+
2168
0+
38Ar
0
√N/pFW (Arbitrary Units)
15.00
10.00
5.00
1.00
1.50
2.00
2.50
3.00
3.50
Kinetic Energy (MeV)
b.)
124Cs
66Ga
123Cs
62Cu
38K
E max (MeV)
5.0
4.0
3.0
2.0
150
200
250
Channel
XBL 8111-1617

Fig. 2

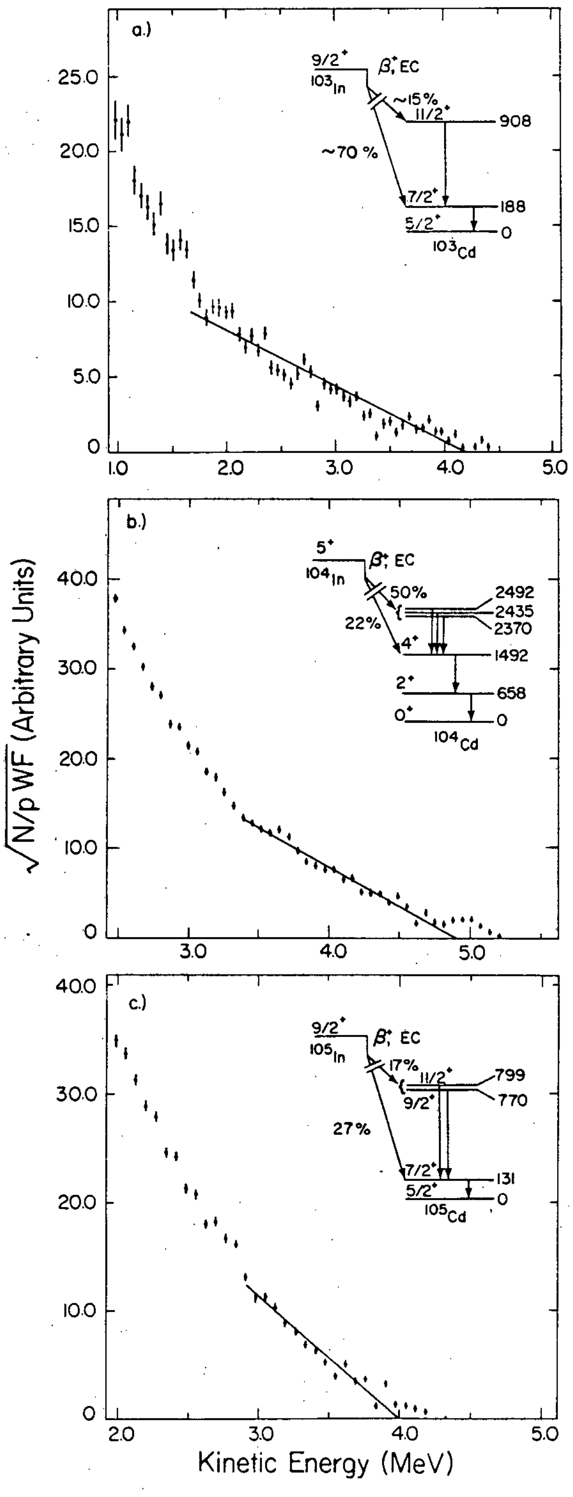

XBL 819-1351

Fig. 3

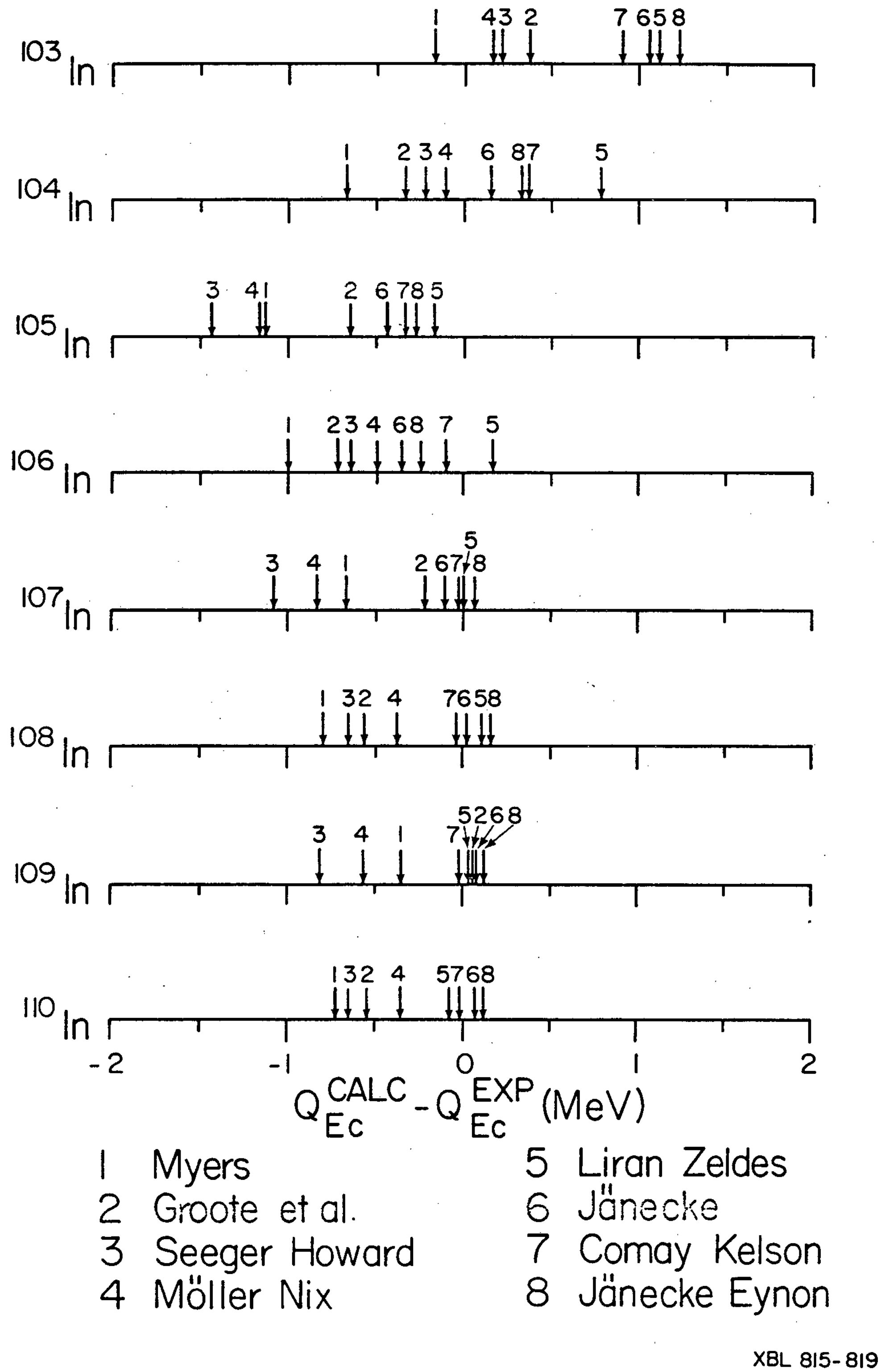

103In
104In
105In
106In
107In
108In
109In
110In
-2
-1
0
1
2
$Q_{Ec}^{CALC} - Q_{Ec}^{EXP}$ (MeV)
1 Myers
2 Groote et al.
3 Seeger Howard
4 Möller Nix
5 Liran Zeldes
6 Jänecke
7 Comay Kelson
8 Jänecke Eynon
XBL 815-819

Fig. 4

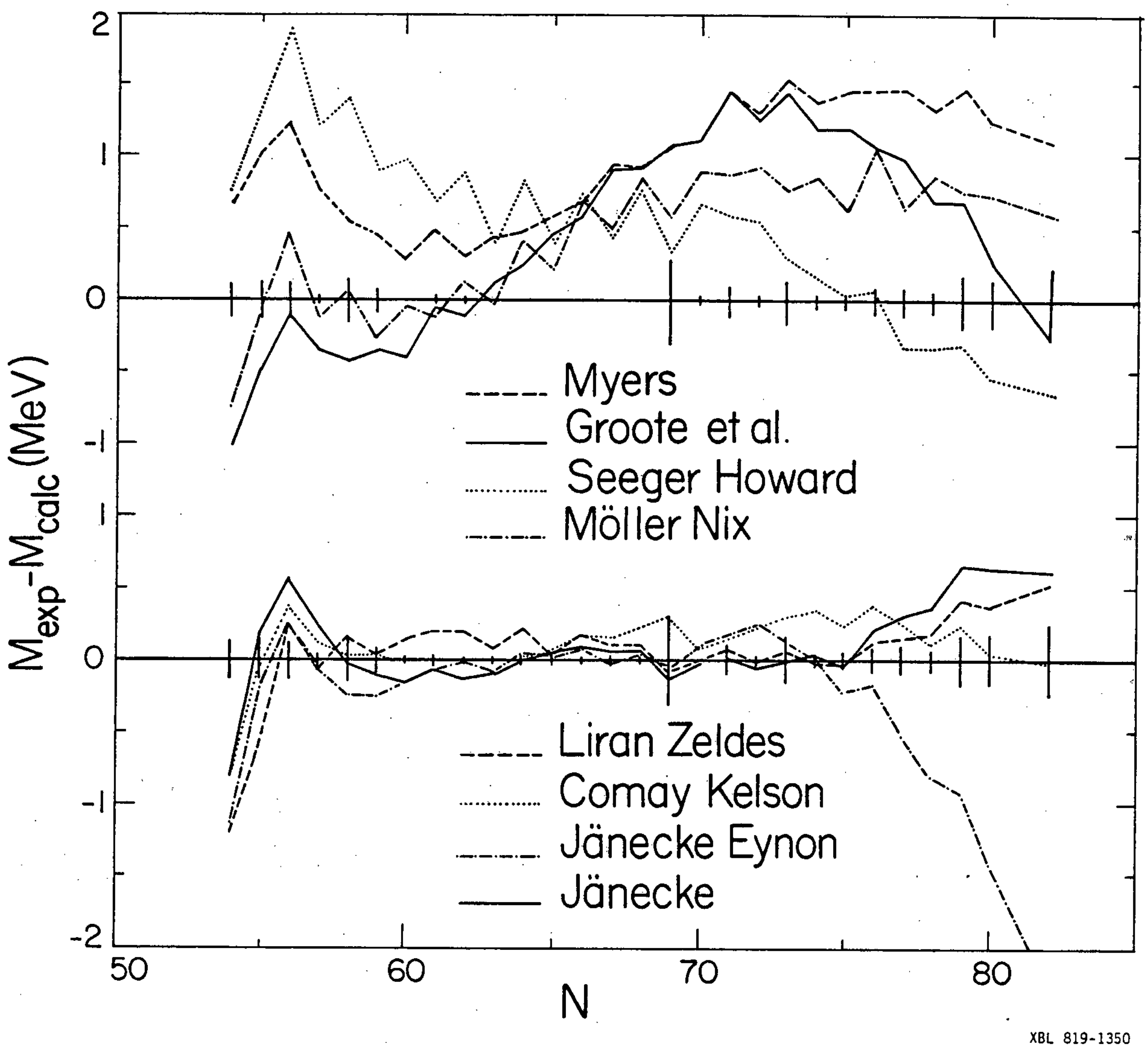

2
1
0
-1
1
0
-1
-2
50
60
70
80
N
M_{exp}-M_{calc} (MeV)
Myers
Groote et al.
Seeger Howard
Möller Nix
Liran Zeldes
Comay Kelson
Jänecke Eynon
Jänecke
XBL 819-1350

Fig. 5

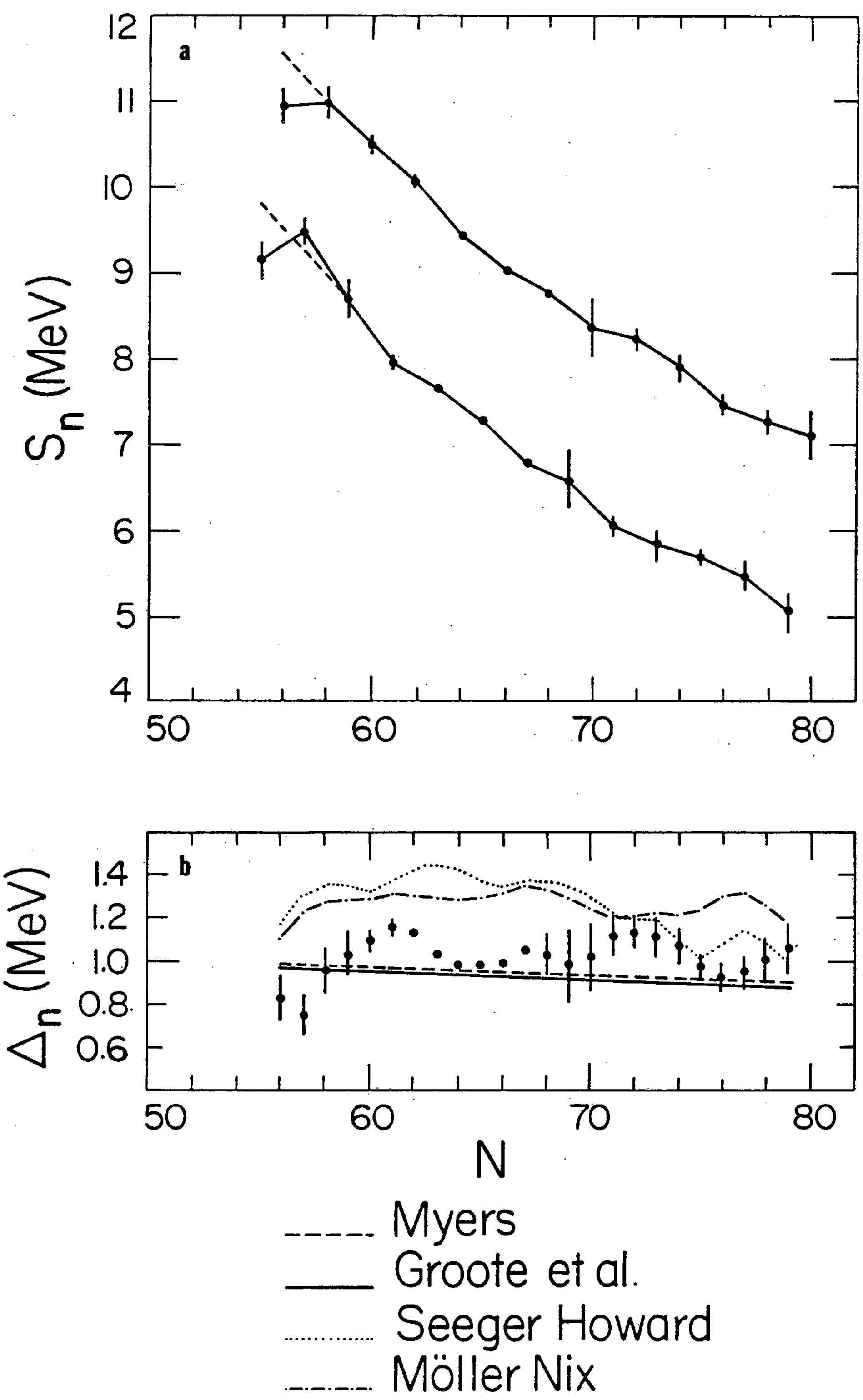

XBL 8110-11944

Fig. 6

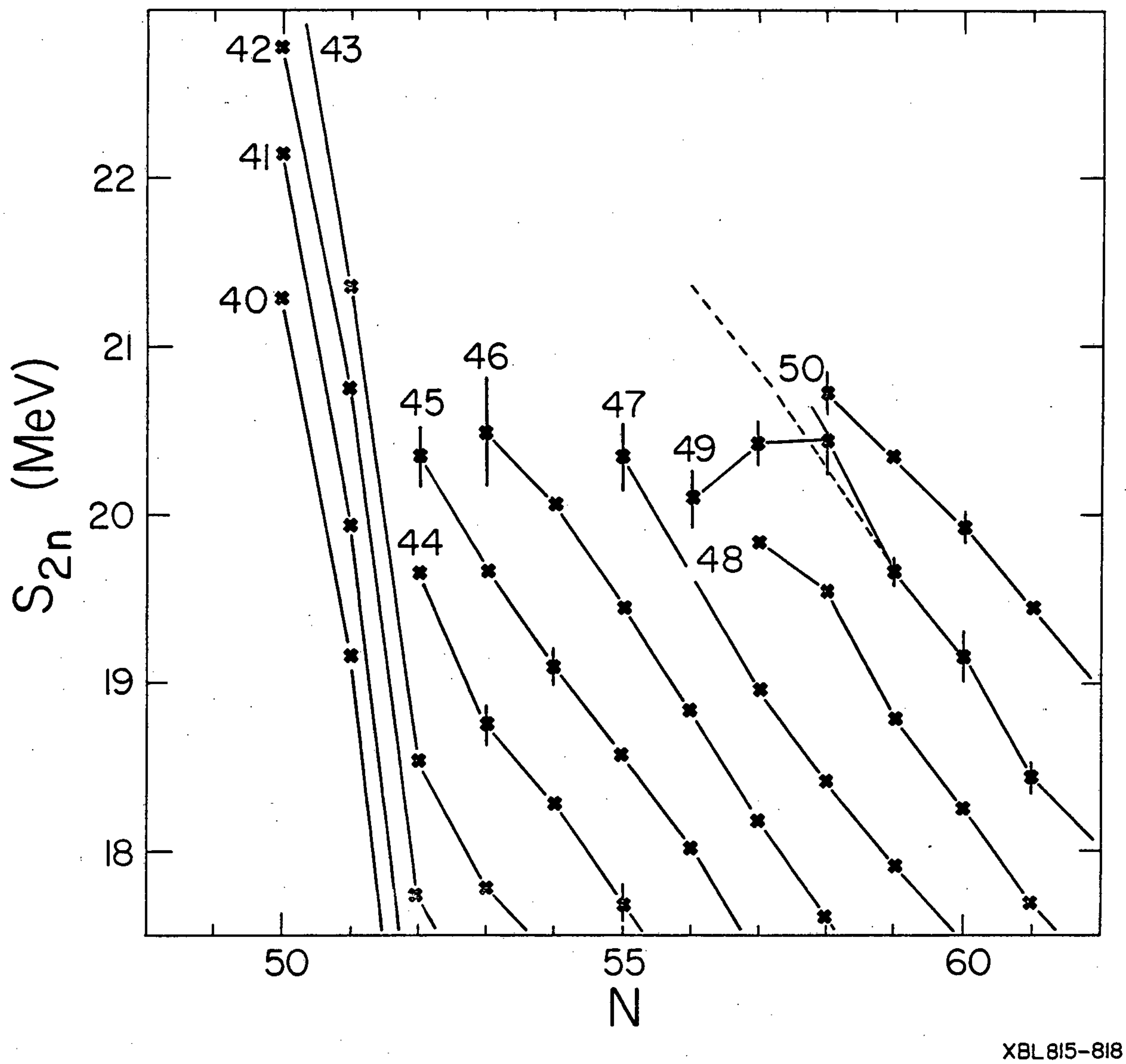
42
43
41
40
46
45
47
50
49
44
48
22
21
20
19
18
S_{2n} (MeV)
50
55
60
N
XBL815-818

Fig. 7

TECHNICAL INFORMATION DEPARTMENT
LAWRENCE BERKELEY LABORATORY
UNIVERSITY OF CALIFORNIA
BERKELEY, CALIFORNIA 94720